Converting topological insulators into topological metals within the tetradymite family

K.-W. Chen,[1,2] N. Aryal,[1,2] J. Dai,[3] D. Graf,[1] S. Zhang,[1,2] S. Das,[1,2] P. Le Fèvre,[4] F. Bertran,[4] R. Yukawa,[5] K. Horiba,[5] H. Kumigashira,[5] E. Frantzeskakis,[3] F. Fortuna,[3] L. Balicas,[1,2] A. F. Santander-Syro,[3] E. Manousakis,[1,2] and R. E. Baumbach[1,2]

[1]*National High Magnetic Field Laboratory, Florida State University, Florida, USA*

[2]*Department of Physics, Florida State University, Florida, USA*

[3]*CSNSM, Universié Paris-Sud, CNRS/IN2P3, Université Paris-Saclay, 91405 Orsay Cedex, France*

[4]*Synchrotron SOLEIL, L'Orme des Merisiers, Saint-Aubin-BP48, 91192 Gif-sur-Yvette, France*

[5]*Photon Factory, Institute of Materials Structure Science, High Energy Accelerator Research Organization (KEK), 1-1 Oho, Tsukuba 305-0801, Japan*

(Received 21 November 2017; revised manuscript received 8 February 2018; published 9 April 2018)

We report the electronic band structures and concomitant Fermi surfaces for a family of exfoliable tetradymite compounds with the formula T_2Ch_2Pn, obtained as a modification to the well-known topological insulator binaries $Bi_2(Se,Te)_3$ by replacing one chalcogen (Ch) with a pnictogen (Pn) and Bi with the tetravalent transition metals T = Ti, Zr, or Hf. This imbalances the electron count and results in layered metals characterized by relatively high carrier mobilities and bulk two-dimensional Fermi surfaces whose topography is well-described by first-principles calculations. Intriguingly, slab electronic structure calculations predict Dirac-like surface states. In contrast to Bi_2Se_3, where the surface Dirac bands are at the Γ point, for $(Zr,Hf)_2Te_2(P,As)$ there are Dirac cones of strong topological character around both the $\bar{\Gamma}$ and $\bar{M}$ points, which are above and below the Fermi energy, respectively. For Ti_2Te_2P, the surface state is predicted to exist only around the $\bar{M}$ point. In agreement with these predictions, the surface states that are located below the Fermi energy are observed by angle-resolved photoemission spectroscopy measurements, revealing that they coexist with the bulk metallic state. Thus this family of materials provides a foundation upon which to develop novel phenomena that exploit both the bulk and surface states (e.g., topological superconductivity).

DOI: 10.1103/PhysRevB.97.165112

I. INTRODUCTION

The compounds Bi_2Se_3 and Bi_2Te_3, which crystallize in the same structure as the naturally occurring mineral "tetradymite" (Bi_2Te_2S [1–3]), have attracted attention as the first examples of three-dimensional topological insulators [4–7]. These and related materials are of interest because their electronic state is gapped in the bulk as in band insulators, but has Dirac-like surface state dispersions which are protected by particle number conservation and time reversal symmetry [8–11]. Hence their electrical transport properties are dictated by the topology of the electronic bands of their surface state instead of a broken symmetry. This leads to protection against a variety of common scattering mechanisms and electrical properties, which are distinct from those of typical metals or insulators [12–16]. Besides topological insulators, a variety of other semimetallic systems exhibit novel behavior resulting from the interplay between symmetry and topology. Well known examples include the Dirac and Weyl semimetals [17–20], although the broader family of topological materials continues to expand [21–23].

An important feature in such materials is whether or not there are tunable parameters to optimize properties, e.g., by varying (i) the nearness of the Fermi level to a Dirac point or (ii) the strength of the spin-orbit coupling to open or close a gap at a Dirac point. In this context, the tetradymite family is a useful template because it can be intercalated with charge dopants [24–26] and also hosts pronounced chemical/structural flexibility. For instance, the minerals "pilsenite" (Bi_4Te_3 [27]) and "tsumoite" (BiTe [28]) are stacking variants within the generalized formula $(Bi_2)_m(Bi_2Te_3)_n$ [3], where Bi_2Te_2Se, Bi_2Te_2S, Bi_2Se_2S, Sb_2Te_2Se, and Sb_2Te_2S are ternary charge balanced variants [1,29–32]. Even elemental bismuth, which exhibits anomalous semimetallic behavior [33], is a member of this family. More recently, Zr_2Te_2P was introduced as a strong topological metal with multiple Dirac cones [34,35]. Zr_2Te_2P is electronically distinct from the $(Sb,Bi)_2(Se,Te)_3$ prototypes: it is not charge balanced, which results in bulk metallic states that coexist with surface Dirac electrons [34]. Here, the proposed topological behavior is due to an avoided crossing between valence and conduction bands whose degeneracy is lifted by the strong spin-orbit coupling from the zirconium ions. This intriguing observation raises several questions including whether bulk metallic states can coexist with topologically protected surface states and, if so, whether the behavior of this composite system is distinct from that of a conventional metal.

In order to probe the electronic phase space for insights to these issues, we synthesized the chemical analogues $(Ti,Zr,Hf)_2Te_2(P,As)$ (abbreviated as "221s"), where the strength of the spin-orbit interaction is systematically varied by replacing Ti → Zr → Hf → and P → As [35]. Band structure calculations for the bulk electronic states show precise agreement with the Fermi surfaces determined from quantum oscillations in the magnetic torque and angle-resolved photoemission spectroscopy (ARPES). The bulk Fermi

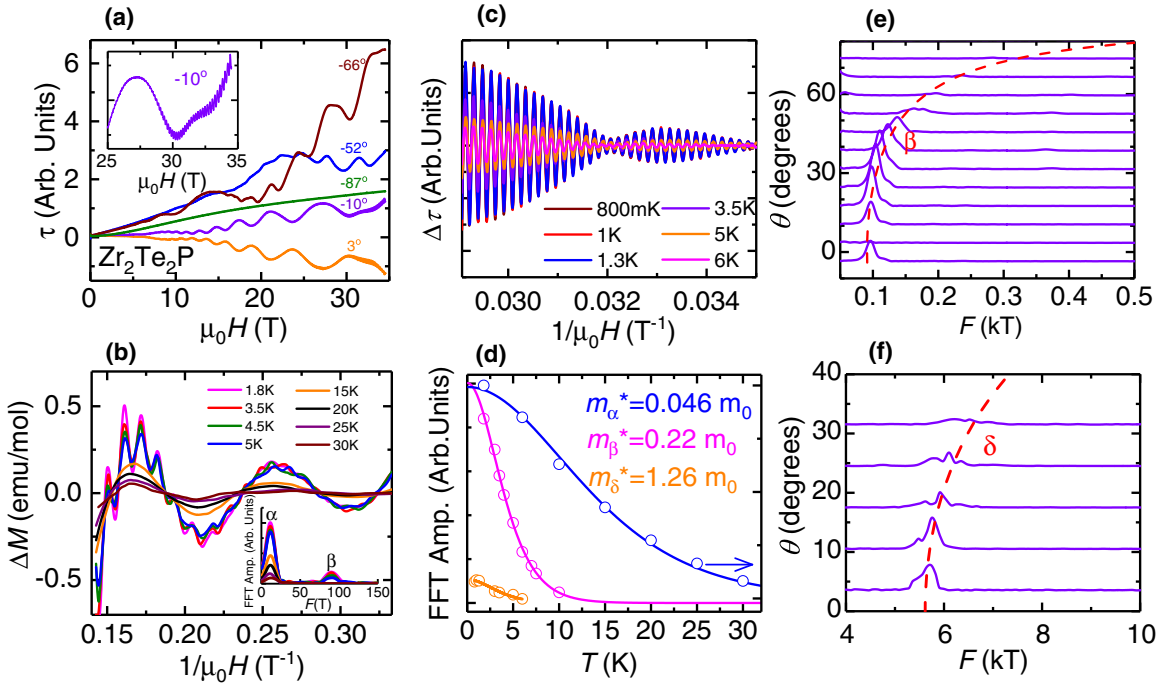

FIG. 1. Summary of quantum oscillation results for Zr_2Te_2P. (a) $\tau(\mu_0 H)$ at various angles θ, where low (main panel) and high (inset) frequency dHvA oscillations are seen. θ is defined as the angle between the crystallographic c axis and $\mu_0 H$, where $\theta = 0^\circ$ and 90° correspond to fields parallel to the c and the a axes, respectively. (b) Taken from Ref. [35]: background subtracted magnetization ΔM vs $\mu_0 H$ showing the low frequency de Haas-van Alphen (dHvA) oscillations for different temperatures. (Inset) Fast Fourier transforms (FFT) for ΔM at various Ts showing the low frequency α and β pockets. (c) Background subtracted $\Delta\tau(\mu_0 H)$ emphasizing the high frequency dHvA oscillations. Another frequency, γ is observed for the Hf_2Te_2P compound, see Fig. S1(f) [36]. (d) Amplitudes of the low and high frequency peaks observed in the FFT spectra as a function of T. Solid lines are fits to the Lifshitz-Kosevich formula from which the effective masses m^* of the charge carriers for different branches are obtained. (e) Fast Fourier transforms of the dHvA signal collected at angles $-40^\circ \leqslant \theta \leqslant 90^\circ$ as functions of the cyclotron frequency F. The red dashed line is a fit to the low frequency orbit β, see main text. (f) Fast Fourier transforms of the dHvA signal collected at angles $0^\circ \leqslant \theta \leqslant 32^\circ$ as functions of the cyclotron frequency F. The red dashed line is a fit to the high frequency orbit δ, see main text.

surfaces are quasi-two-dimensional and are characterized by relatively high charge carrier mobilities. Calculations predict the presence of composition dependent and topologically protected surface states within their Brillouin zone (BZ). Angle-resolved photoemission spectroscopy measurements uncover Dirac-like electronic dispersions on the surface of these materials in broad agreement with these predictions. These results allow us to understand how variations in the spin orbit coupling controls the electronic behavior and set the stage to systematically tune the electronic state.

Importantly, the conversion from topological insulator to a strong topological metal is achieved not through chemical substitution, which would introduce disorder, but rather in stoichiometric materials with nearly perfect crystalline order. This enables the surface states, which have a strong topological character, to realize their "robust" nature and suggests that the 221s are hosts for potential fundamental discoveries and applications, including: (i) superlattices of these materials could serve as platforms for topological superconductivity due to the proximity effect, where the necessary metallic component is intrinsic to the system. (ii) Since there are active topological surface states corresponding to a high symmetry point of the Brillouin zone that are close to the Fermi energy, it is possible to study the resulting two dimensional electron gas and its phases. (iii) The interplay between the surface and bulk Fermi sea might produce novel phenomena. (iv) Chemical substitution or intercalation could be used to vary the Fermi energy or the band structure. For instance, the transition from Zr_2Te_2P to Ti_2Te_2P is of interest because the former hosts a surface state with strong topological character at the zone center while the latter does not. (v) Any one of these materials or their chemical variants might be useful as components in junction devices. Thus the 221s represent a deep reservoir for novel physics and have the advantage that their experimentally measured electronic state is fully understood via electronic structure calculations, bringing a design-based methodology within reach.

The paper is organized as follows. In Sec. II A, we present the results of our quantum oscillation experiments (QOE). In Sec. II B, we give the results for the Fermi surface of these materials as revealed by our DFT calculations, the QOE and ARPES. Section II C we present our results and topology of the bands as obtained by our DFT calculations and verified by ARPES. In Sec. III, we discuss the implications of our experimental and theoretical findings and in Sec. IV, we present our conclusions.

II. RESULTS

A. Quantum oscillation experiments

The Fermi surface topographies and the associated bulk charge carrier properties were probed using torque

TABLE I. Summary of the properties extracted for the α, β, γ, and δ branches of the dHvA signal from Zr_2Te_2As, Zr_2Te_2P, and Hf_2Te_2P. Quantum oscillatory frequencies F(T), charge-carrier effective masses $m^*(m_e)$, Dingle temperatures T_D(K), and Fermi wave vectors $k_F(nm^{-1})$ are tabulated.

	α_{ZrP}	α_{HfP}	β_{ZrAs}	β_{ZrP}	β_{HfP}	γ_{HfP}	δ_{ZrP}	δ_{HfP}
F(T)	11	107	46	90	149	460	5800	5670
$m^*(m_e)$	0.046	0.27	0.1	0.2	0.22	–	1.26	1.1
T_D(K)	19	15	23	11	6.5	–	–	–
k_F (nm^{-1})	0.18	$k_{ab} = 0.56$ $k_c = 2.08$	0.37	0.52	0.67	1.18	4.2	4.15

magnetometry $\tau(\mu_0 H)$ measurements (Fig. 1 and Fig. S1 [36]), which reveal de Haas van Alphen (dHvA) oscillatory signals for Zr_2Te_2P, Hf_2Te_2P, and Zr_2Te_2As. Measurements were made at select angles θ between an external magnetic field $\mu_0 H$ and the crystallographic c axis. $\tau(\mu_0 H)$ was also measured for Ti_2Te_2P (not shown) but no dHvA signal is present, which is likely due to a lower sample quality or differences in the Fermi surface. The results for Zr_2Te_2P, Hf_2Te_2P, and Zr_2Te_2As are qualitatively similar and in the main text we focus on Zr_2Te_2P.

Several families of oscillations labeled α, β, and γ are identified for $F < 500$ T, and close to $\theta = 0^\circ$ there is another group of high frequency oscillations ($F \approx 5$–6 kT) labeled δ for Zr_2Te_2P and Hf_2Te_2P. Together, these results reveal two distinct sets of Fermi surface sheets, as summarized in Table I, that are in good agreement with the expectations from electronic structure calculations where α, β, and γ are associated with the "cigar" and "gear" hole pockets and δ with the large electron pockets (see Sec. II B and Fig. 2 for definitions from electronic structure calculations). The angle dependencies of the β and δ frequencies are shown in Figs. 1(e) and 1(f) and both are described by the expression $F_{\beta,\delta}(\theta) = F(0)/\cos\theta$, as expected for cylindrically shaped Fermi surfaces. Earlier work revealed a cylindrical α branch for Zr_2Te_2P [35], but this feature is less prominent in the measurements shown here. Also note that an α orbit has not yet been seen for Zr_2Te_2As. For Hf_2Te_2P, the α orbit is best described by an ellipsoidal FS and an additional frequency F_γ appears at limited angles. The Fermi wave numbers k_F resulting from these fits are summarized in Table I.

Insight into the nature of the charge carrier quasiparticles is gained by considering the temperature dependence of the dHvA signal amplitude A [Fig. 1(d)]. The $A(T)$ curves are described by the Lifshitz-Kosevich (LK) expression for a Fermi liquid, where fits yield typical bare electron masses m_δ for the δ orbit and small effective masses m_α and m_β for the small α and β orbits, respectively (results for all three compounds are summarized in Table I). This reveals that while the α and β pockets have band masses similar to those seen in other topological materials, the large δ pockets are more conventional in nature. Particularly noteworthy is the very small mass that is observed for the α pocket in Zr_2Te_2P ($m_\alpha = 0.046\, m_e$).

B. Electronic Fermi surface

We next discuss the calculated Fermi surfaces (FS) determined from density functional theory (DFT) and compare with results from QO and ARPES measurements. The FS of Zr_2Te_2P in the rhombohedral unit cell is shown in Fig. 2(a), and similar representations for the other three compounds are shown in Ref. [36] (see Fig. S5). The large "petal"-like electron sheets (blue) are similar in all 4 compounds. In Figs. 2(b) and 2(c), the projected Fermi surfaces on the $k_x - k_y$ and $k_x - k_z$ planes as measured by ARPES are shown for comparison with the DFT, where there is strong agreement. In addition, the quasi-2D Fermi surface structure is confirmed by the measured out-of-plane ARPES Fermi-surface map, shown in Fig. 2(c). There are also "hole" pockets (red) around the Γ point, which differ between the four materials [Figs. 2(d)–2(g)]. The wavy features of some of the hole pockets are artifacts of the finite k-point mesh and the interpolation scheme used in the

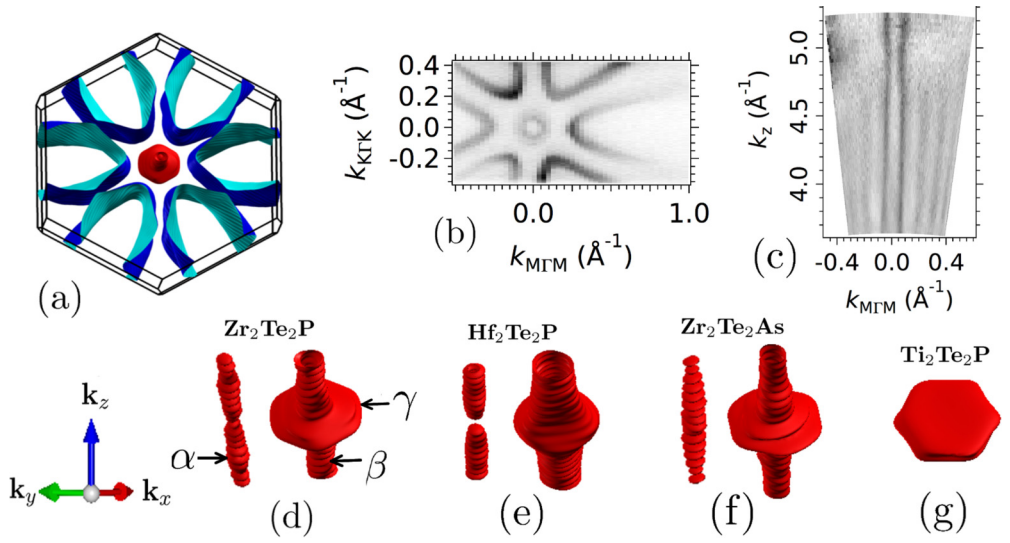

FIG. 2. Fermi surface sheets calculated from density functional theory (DFT): (a) calculated full Fermi surface for the Zr_2Te_2P. (b) The projected Fermi surface on the k_x-k_y plane as measured by ARPES. (c) The projected Fermi surface on the k_x-k_z plane as measured by ARPES. (d), (e), (f), and (g) are, respectively, the Zr_2Te_2P, Hf_2Te_2P, Zr_2Te_2As, and Ti_2Te_2P hole pockets around the Γ point.

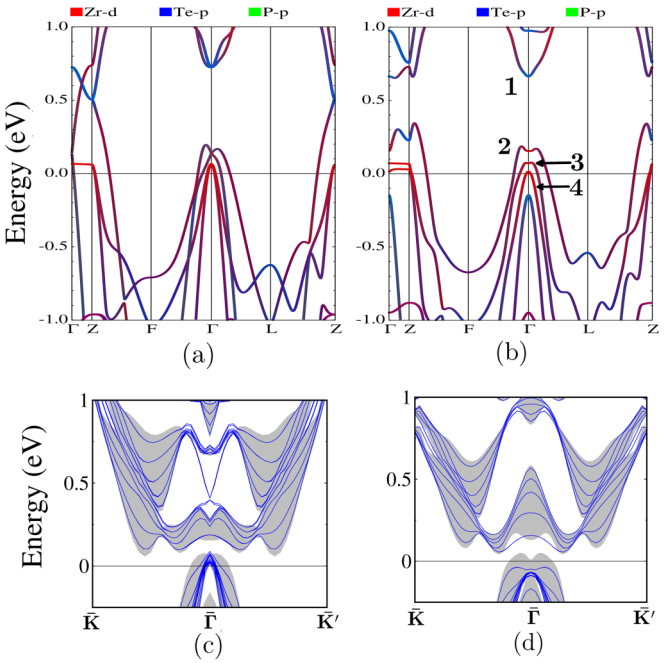

FIG. 3. Band structure of Zr_2Te_2P in the rhombohedral unit cell along the TRIMs (a) without the inclusion of the spin-orbit coupling (SOC) and (b) with the inclusion of SOC. The colors used indicate the orbital character of the bands: red, blue, and green colors corresponds to Zr d, Te p, and P p orbitals, respectively. The superposition of bulk bands (shown as Gray ribbons) with bands obtained from a slab of five quintuple layers (shown as blue lines) depicting the presence of a Dirac-like surface state at the $\bar{\Gamma}$ point is shown for Zr_2Te_2P in (c). (d) shows the absence of such a surface state for Ti_2Te_2P at the $\bar{\Gamma}$ point.

XCRYSDEN software [37]. We have shown (see Fig. S7 [36]) that they can be removed by using Wannier interpolation but it is computationally costly. As seen in Figs. 2(d)–2(g) there is a hole pocket, which can be identified as "cigar"-like and another hole pocket, which can be identified as "gear"-like. The cigar and gear pockets correspond to the two bands at the Γ point (labeled as 4 and 3, respectively, in Fig. 3), which intersect the Fermi surface for Zr_2Te_2P, Zr_2Te_2As, and Hf_2Te_2P. In the case of Ti_2Te_2P the lowest of the two bands sinks in the Fermi sea, and the cigarlike pocket disappears. For the Hf-based compound this lowest band is also below the Fermi level at the Γ point; however, for $\vec{k}$ near the high-symmetry point A (0,0,1/2) of the hexagonal Brillouin zone boundary, this band moves above the Fermi level as is the case for Zr_2Te_2P and Zr_2Te_2As.

The calculated values of the orbits, corresponding to extremal cross-sectional areas of the Fermi surface, viewed along the hexagonal c axis are listed in Table II. The cigar-shaped hole pocket has one minimum orbit at Γ and another one at the A (0,0,1/2) high-symmetry point of the hexagonal BZ and a maximum at (0,0,1/4) [shown as α in Fig. 2(d)]. The gear-shaped hole pocket has a maximum at Γ [shown as γ in Fig. 2(d)] and one minimum orbit at (0,0,1/2) [shown as β in Fig. 2(d), which corresponds to the "gear shaft"]. Notice that the Ti-based compound is missing all the orbits which correspond to the cigar shaped hole pocket. In addition, the Hf-based material is missing the minimal orbit at $k_z = 0$.

TABLE II. Calculated extremal cross-sectional areas for the electron pockets of all four compounds in units of tesla.

FS pocket	Zr_2Te_2P	Zr_2Te_2As	Hf_2Te_2P	Ti_2Te_2P
"cigar" ($k_z = 0$)	26(3)	13(1)	0	0
"cigar" ($k_z = 1/4$)	45(1)	49(1)	49(27)	0
"cigar" ($k_z = 1/2$)	26(3)	13(1)	49(27)	0
"gear" ($k_z = 1/2$)	60(16)	52(9)	172(28)	0
"gear" ($k_z = 0$)	792(176)	596(192)	843(99)	863(50)
e-sheet ($k_z = 0$)	3805	3599	4158	3641
e-sheet ($k_z = 1/4$)	7874	7226	7607	6349
e-sheet ($k_z = 1/2$)	6553	5790	6463	7059

The gear-shaped hole pocket gives rise to a small (<100 T) orbit and a medium (several hundred tesla) orbit. The electron sheets give rise to three different large orbits, which correspond to intersections to the hole pocket at (0,0,0), (0,0,1/4), and (0,0,1/2).

The DFT calculations correctly predict the general characteristics of the Fermi surface sheets as seen by our quantum oscillation experiments. As shown in Table II, the calculations predict three very large electron pockets with frequency in the range of 4000–7000 T and the quantum oscillation experiments in Table I also reveal frequencies at around 6000 T. There are several much smaller-size hole orbits originating from the extrema of the two hole-pocket sheets, which are due to their shape shown in Figs. 2(d)–2(f). From the size of these frequencies and their angular dependence we can identify the frequencies labeled α and β in the angular dependence of the QO measurements. In both the calculation and the experimental results, the "cigar"-like hole pocket is absent in the case of the Ti-based compound. This is confirmed by ARPES measurement as shown in Figs. 4(c) and 4(d). The band is still present in the Ti-based compound but the pocket is "pushed" below the Fermi level. In addition, the "gear"-like pocket for the Ti-based compounds loses its "shaft." We note that in going from Zr_2Te_2P to Zr_2Te_2As, the frequency of the small hole pockets is reduced in both the experimental results and in our computations. We also find that in the case of the Hf-based compound the "cigar"-like hole pocket misses the lowest orbit at Γ because the "cigar" thickness at Γ seems to vanish.

In the case of the Hf-based compound, there is an additional hole pocket (labeled γ, see Fig. S1 (f) [36]) with frequency at around 450 T that is observed experimentally. This orbit could correspond to the hexagonal-shaped maximum orbit obtained in all compounds from the "gear"-like shaped hole pocket in the DFT calculations [labeled as γ in Fig. 2(d)] with a frequency in the range of 500–900 T. Its precise value is very sensitive to very small adjustments of the Fermi surface and the discrepancy from the experimental value should not be taken seriously. Furthermore, its absence from the other compounds may be due to a lack of the required experimental sensitivity, as even in the Hf-based compound it is difficult to detect.

C. Electronic band structure

The calculated band structures, with and without spin-orbit coupling (SOC), along with their orbital character for Zr_2Te_2P

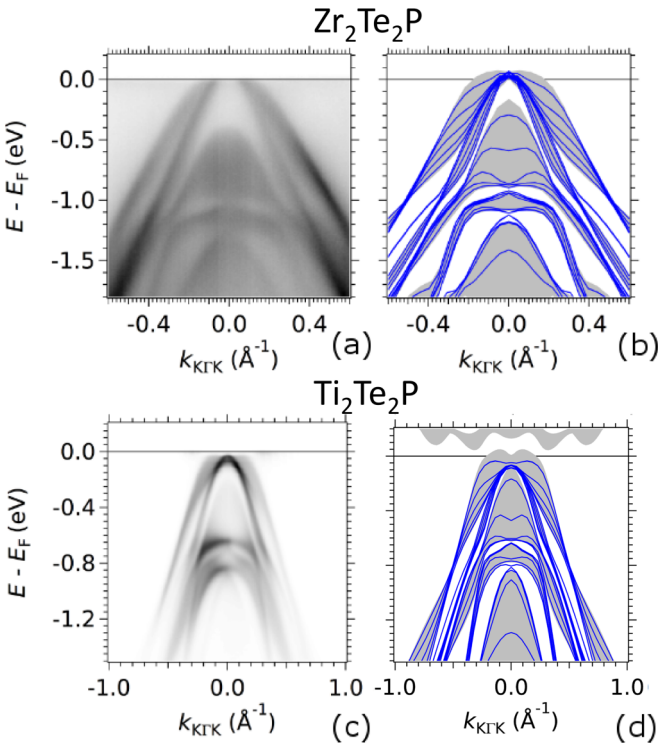

FIG. 4. Comparison between ARPES measurements and band-structure calculations for cuts along the K-Γ-K direction. (a) ARPES determined band dispersion and (b) calculated DFT bands for Zr_2Te_2P, respectively. (c) ARPES and (d) DFT for Ti_2Te_2P, respectively. Fermi energy E_F is indicated by the horizontal black line. Blue solid lines are bands obtained from a five-layer slab calculation and therefore represent surface states and grey ribbons represent the bulk bands.

are presented in Figs. 3(a) and 3(b). A first indication of the presence of nontrivial topology is seen by comparing the band structure with and without SOC. Between bands 1 and 2, which are of Zr d and Te p orbital character, at the time-reversal invariant momentum (TRIM) Z, which projects onto the $\bar{\Gamma}$ point of the hexagonal BZ in our slab calculation and in the notation of our ARPES measurements, there is a band inversion similar to what is seen for Bi_2Se_3, although in the latter case the orbitals involved in the band inversion are of p character, which form bands of different parity at the **Γ** point [4]. In addition, at the TRIM L (which projects onto the $\bar{M}$ point of the hexagonal BZ), there is parity inversion between bands 2 and 3. Notice that these two bands are made of Te p orbitals as in the Bi_2Se_3 case. Similar features are found for the Zr_2Te_2As and Hf_2Te_2P compound. In the case of the Ti_2Te_2P compound, while there is parity inversion at the $\bar{M}$ point, there is no inversion at the $\bar{\Gamma}$ point. As a result all our compounds have a topological surface state between bands 2 and 3 at the $\bar{M}$ point and at the $\bar{\Gamma}$ all other compounds have a topological surface state between the aforementioned two bands with the exception of the Ti-based one. Figures 3(c) and 3(d) present the bulk bands (shown as gray ribbons) with bands obtained from a slab calculation (shown as blue lines) depicting the presence of a Dirac-like surface state at the $\bar{\Gamma}$ point in Zr_2Te_2P in panel (c) and the absence of such a surface state for Ti_2Te_2P at the $\bar{\Gamma}$ point (see Figs. S8 and S9 [36] for the surface states in Hf_2Te_2P). The Ti-based compound does not have strong enough SOC to cause band inversion at the $\bar{\Gamma}$ point; at the $\bar{M}$ point, however, the band character in all compounds, including the Ti-based one, is Te p type for which the SOC is strong enough to cause band inversion.

In order to investigate whether or not the Dirac surface states seen in ARPES and slab calculation have strong topological character, we performed parity analysis of the bulk bands following Ref. [38], which is simplified because of the presence of inversion symmetry in the 221 structure. We first focus on the surface state around the $\bar{\Gamma}$ point that is present in Zr_2Te_2P and Hf_2Te_2P but is absent in Ti_2Te_2P [see Figs. 3(c) and 3(d)], as was done previously in Ref. [34]. We find the parity product of all the occupied bands (10 pairs) below band 1. In this calculation, we neglect the deeply situated bands (not shown) which are separated from the higher occupied bands by an energy gap. For Zr_2Te_2P and Hf_2Te_2P, the parity product at the TRIMs around the Γ, F, L, and Z points within the BZ [4] are respectively positive, positive, positive and negative whereas the parity product for all the TRIMs in Ti_2Te_2P is positive. This gives a Z_2 topological index $\nu_0 = 1$ for Zr_2Te_2P and Hf_2Te_2P, whereas $\nu_0 = 0$ for Ti_2Te_2P. This implies that there are an odd number of surface states between bands 1 and 2 for Zr_2Te_2P and Hf_2Te_2P and that they are robust to external perturbations [38], whereas there are even (or zero) number of surface states for Ti_2Te_2P which are not robust. Note that the TRIM Z, where parity inversion is seen, projects onto the $\bar{\Gamma}$ point in the hexagonal Brillouin zone. We refer the reader to Refs. [4,34] for an illustration of how the rhombohedral BZ projects onto the 2D hexagonal BZ.

A similar analysis was performed to investigate the topology of the surface state seen between bands 2 and 3, i.e., those leading to the "petals" and the "gear"-like FSs, respectively, at the $\bar{M}$ point. From this analysis, we find $\nu_0 = 1$ for Zr_2Te_2P and Ti_2Te_2P, whereas $\nu_0 = 0$ for Hf_2Te_2P. For Zr_2Te_2P and Ti_2Te_2P, the parity product is negative only at the TRIM L which projects onto $\bar{M}$ point of the hexagonal BZ, whereas for Hf_2Te_2P the parity product is negative at the two TRIMs Z and L. This makes the overall product positive and results in a Z_2 index of 0. Thus we expect that for Zr_2Te_2P and Ti_2Te_2P, there are odd numbers of Dirac-like states (three at the L points, which projects onto the $\bar{M}$ point of the hexagonal Brillouin zone of the slab) and for Hf_2Te_2P, there are even number of Dirac-like states (one at the $\bar{\Gamma}$ point and three at the $\bar{M}$ point) between the electron band and the "gear" band. Therefore, for Hf_2Te_2P, the parity analysis shows that the surface Dirac band at the $\bar{M}$ point does not have strong topological character because the parity inversion happens at both the Z and L point as stated above.

Figure 4 shows a comparison between the surface band structure measured by ARPES and the one calculated by DFT for both Zr_2Te_2P [panels (a) and (b)] and Ti_2Te_2P [panels (c) and (d)] along the $\bar{K}$-$\bar{\Gamma}$-$\bar{K}$ direction. Holelike states are observed in both cases, which agree well with the calculated ones. Likewise, Fig. 5 compares the measured (ARPES) and calculated (DFT) surface band structure for the same two compounds along the $\bar{K}$-$\bar{M}$-$\bar{K}$ direction. In both cases, a Dirac cone, with its vertex located at around 1 eV below E_F for Zr_2Te_2P (0.82 eV below E_F for Ti_2Te_2P), is observed in the

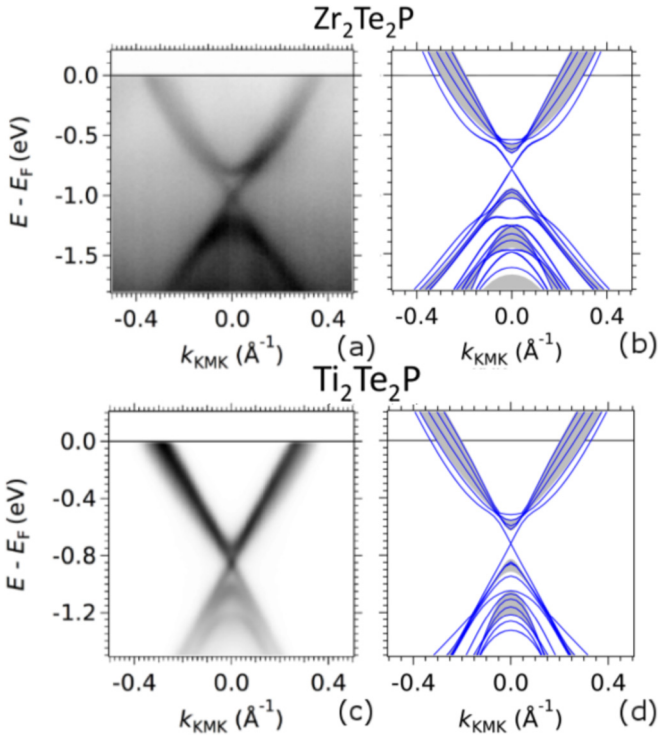

FIG. 5. Comparison between ARPES measurements and band structure calculations for cuts along the K-M-K direction. (a) ARPES determined band dispersion and (b) calculated DFT bands for Zr_2Te_2P, respectively. (c) ARPES and (d) DFT for Ti_2Te_2P, respectively. Fermi energy E_F is indicated by horizontal line. Solid blue lines depict bands obtained from a five-layer slab calculation and represent surface states and grey ribbons represent the bulk bands.

ARPES data [panels (a) and (c)]. The same Dirac cone is predicted by DFT [panels (b) and (d)].

As seen in Figs. 4 and 5, the ARPES and DFT band structure is in good agreement, especially close to the Fermi level. Moreover, the presence or absence of certain hole pockets, such as the "cigar" or "gear"-like pockets, moving from one material studied to other, can be verified by examining the intersection of the ARPES bands with Fermi surface as predicted by the DFT calculations and seen in our QO experiments. We highlight the absence of the "cigar"-like pocket for Ti_2Te_2P as correctly predicted by DFT and confirmed by ARPES.

For the bands away from the Fermi level, the DFT calculations have to be down-shifted with respect to the ARPES ones by 100–200 meV with this shift being not rigid. For instance, between the $\bar{K}$-$\bar{\Gamma}$-$\bar{K}$ and $\bar{K}$-$\bar{M}$-$\bar{K}$ directions, the amount of shift is compound dependent. We, however, note that the energy position of the bands crossing E_F is almost unchanged in ARPES and DFT. Surface band bending effects—typical in tetradymite topological insulators [39–41]—may be at the origin of such energy shifts of the experimental bands. In any case, such a shift is a purely extrinsic effect that does not change our main analysis and conclusions. The results for Hf_2Te_2P are summarized in Ref. [36], where the measured Fermi surfaces for all samples are also shown. For all three compounds there is a good agreement between the calculated and the measured bulk bands, while the out-of-plane Fermi surface of Zr_2Te_2P confirms the two-dimensional character of the bands [see Fig. 2(c)] as suggested by our QO measurements. We therefore conclude that the Fermi level found from the self consistent calculation of the Kohn-Sham Hamiltonian gives the best agreement between theory and experiment.

III. DISCUSSION

Our results comprehensively characterize the electronic states of the layered tetradymite metals $(Ti,Zr,Hf)_2Te_2(As,P)$ and the impact of changing the spin-orbit coupling through stoichiometric chemical variations. In the bulk, there are both hole and electron pockets which all have close to cylindrical topography, as revealed by electronic structure calculations, the de Haas-van Alphen effect, and ARPES measurements. The hole pockets are small in volume with their associated charge carriers characterized by light cyclotron masses. The electron sheets are larger with effective masses that are similar to the bare electron mass. Intriguingly, the slab calculations predict linearly dispersing surface states of strong topological character (as shown from parity analysis) above the Fermi energy at the $\bar{\Gamma}$ point for the Hf and Zr versions and below the Fermi energy at the $\bar{M}$ point for all chemical variants, which are indeed observed by ARPES measurements. Therefore the 221 materials are shown to be an attractive family of materials in which to develop novel phenomena that exploit both the bulk and surface states, where electronic structure calculations provide quantitative guidance for designing specific band structures.

A main interest is to induce superconductivity by tuning the electronic state. There are several possible routes to do this, but an attractive way is through the proximity effect [42]. This is feasible in the 221s because, similar to the more studied $Bi_2(Se,Te)_3$ topological insulators, these compounds are exfoliable [35]. This makes them candidates for fabricating heterostructures containing superconducting leads or for inducing superconductivity through ionic liquid gating [43,44]. That being said, topological metals are also a natural environment for bulk superconductivity to coexist with protected surface states, without having to create an artificial structure. Noteworthy current examples include $PbTaSe_2$ [45] and some intercalated variants of the closely related prototypical topological insulators $Bi_2(Se,Te)_3$ [24,25]. We point out that the 221s provide an even more advantageous setting to develop topological superconductivity because (i) their band structure is fully characterized and, hence, Fermi surface design is viable and (ii) topological states are present at both the Γ and $\bar{M}$ points. This opens the door to multiple unique superconducting gaps and nontrivial pairing symmetries. Importantly, at the Γ point, the Dirac cones are only 200 meV, 400 meV away from the Fermi energy for Hf_2Te_2P and 400 meV for Zr_2Te_2P. This is within the reach of common experimental tuning parameters (e.g., intercalation, chemical substitution, electronic gating, exfoliation and applied pressure), making access to these cones a practical goal. It is also useful that the Ti analogue does not host a Dirac cone at the Γ point, which will help to identify behavior that is associated with this group of Dirac cones in the Zr and Hf analogues. The $\bar{M}$ point surface states are more distant from the Fermi energy in the current generation materials, but we point out that it is not necessary to reach the tip of the Dirac cone in order to access the associated protected

states. Therefore we expect that even here the Fermi energy can be sufficiently moved using routine strategies. In other words, these compounds offer a design based environment in which to induce novel and perhaps topological superconducting states from different subsets of charge carriers with distinct properties.

Even if superconductivity is not induced, there are opportunities relating to the Dirac cones at the Γ or $\bar{M}$ points. In the current materials, our calculations show that when the sample is made a few layers thick (e.g., through exfoliation), the finite momenta bulk states are discrete and the ratio of surface to bulk is non-negligible. In this situation, the decay of the surface states into the bulk would be avoided and functionalities that go beyond that of topological insulators might emerge. An early perspective on how this might occur is seen in work addressing interface states of the topological insulator with metals where the metallic bands acquire topological character, e.g., resulting in a spin-transfer torque generator [46]. There also has been work addressing emergent functionality when a Dirac cone and a two-dimensional electron gas are confined to the same region [39,47]. For the 221s, the parabolic band at the $\bar{M}$ point is two dimensional and is in close vicinity to the associated Dirac point. This again sets the stage to induce novel interactions between surface and bulk states. We point out that, so far, many such applications have been proposed for topological insulators, but there are some important obstacles. In particular, nontrivial challenges include (1) that very high quality specimens must be available, where bulk impurity states do not intrude on the very narrow energy gaps that characterize most known topological insulators and (2) that the technical capability to make the junction should be easily implemented. For hybrid materials like the 221s, these complications may be avoided because the hierarchical electronic composite intrinsically combines tunable surface and bulk states. Finally, it is even true that trivial surface states on metals have attracted significant attention spanning fundamental physics [48,49] to surface chemistry [50,51]. It remains to be seen how the presence of topologically protected surface states on metals will drive progress in these fields. Therefore, in these and other areas, we anticipate that the introduction of this new class of topological metals will naturally lead to discoveries.

IV. SUMMARY

We have studied a family of strongly topological metals with the chemical formula T_2Ch_2Pn (T = Ti, Zr, Hf), which are characterized by nearly perfect crystalline order. The electronic band structures and Fermi surfaces for these materials are reported based on electronic structure calculations, quantum oscillations in torque magnetometry, and angle-resolved photoemission spectroscopy. The bulk Fermi surface consists of hole and electron pockets which are all nearly two dimensional. The electron sheets are conventional in nature, while the hole pockets have small cyclotron masses. Intriguingly, the slab electronic structure calculations predict topologically protected Dirac-like surface states at two distinct locations within their Brillouin zone. Of these states, those located below the Fermi level are observed by our angle-resolved photoemission spectroscopy measurements which are in good agreement with DFT calculations.

These materials provide a platform on which to study surface states of strong topological character in coexistence with a bulk metal. This suggests many potential applications, where an attractive possibility is that they could host topological superconductivity following different tuning strategies, e.g., via the proximity effect or through electronic tuning of the bulk using standard strategies. Even if superconductivity does not appear there are attractive features associated with the Γ and $\bar{M}$ point Dirac cones, which are also practical to access using the same tuning strategies. We furthermore suggest that topological metals may even present some advantages over the better studied topological insulator analogues in certain applications. In particular, if an interface of a topological insulator with a metal is needed for a particular application, there are challenges associated with impurity states due to lattice mismatch or due to doping. Construction of such interfaces are avoided in hybrid crystalline materials like the 221s because the hierarchical electronic composite intrinsically combines tunable surface and metallic bulk states. Therefore, with the comprehensive understanding from calculations and experiment, it is now possible to envision developing a design-based strategy to harness novel behavior in topological metals.

ACKNOWLEDGMENTS

This work was performed at the National High Magnetic Field Laboratory (NHMFL), which is supported by National Science Foundation Cooperative Agreement No. DMR-1157490, the State of Florida and the DOE. A portion of this work was supported by the NHMFL User Collaboration Grant Program (UCGP). L.B. is supported by DOE-BES through award DE-SC0002613. The work at KEK-PF was performed under the approval of the Program Advisory Committee (proposals 2016G621 and 2015S2-005) at the Institute of Materials Structure Science.

K.-W.C. and N.A. contributed equally to this work.

[1] L.-L. Wang and D. D. Johnson, Ternary tetradymite compounds as topological insulators, Phys. Rev. B **83**, 241309(R) (2011).

[2] D. Harker, The crystal structure of the mineral Tetradymite Bi_2Te_2S, Z. Kristallogr. - Crystalline Materials **89**, 175 (1934).

[3] J. W. G. Bos, H. W. Zandbergen, M.-H. Lee, N. P. Ong, and R. J. Cava, Structures and thermoelectric properties of the infinitely adaptive series $(Bi_2)_m(Bi_2Te_3)_n$, Phys. Rev. B **75**, 195203 (2007).

[4] H. Zhang, C.-X. Liu, X.-L. Qi, X. Dai, Z. Fang, and S.-C. Zhang, Topological insulators in Bi_2Se_3, Bi_2Te_3 and Sb_2Te_3 with a single Dirac cone on the surface, Nat. Phys. **5**, 438 (2009).

[5] Y. L. Chen, J. G. Analytis, J.-H. Chu, Z. K. Liu, S.-K. Mo, X. L. Qi, H. J. Zhang, D. H. Lu, X. Dai, Z. Fang, S. C. Zhang, I. R. Fisher, Z. Hussain, and Z.-X. Shen, Experimental realization of

a three-dimensional topological insulator Bi_2Te_3, Science **325**, 178 (2009).

[6] D. Hsieh, Y. Xia, D. Qian, L. Wray, J. H. Dil, F. Meier, J. Osterwalder, L. Patthey, J. G. Checkelsky, N. P. Ong, A. V. Fedorov, H. Lin, A. Bansil, D. Grauer, Y. S. Hor, R. J. Cava, and M. Z. Hasan, A tunable topological insulator in the spin helical Dirac transport regime, Nature (London) **460**, 1101 (2009).

[7] Y. Xia, D. Qian, D. Hsieh, L. Wray, A. Pal, H. Lin, A. Bansil, D. Grauer, Y. S. Hor, R. J. Cava, and M. Z. Hasan, Observation of a large-gap topological-insulator class with a single Dirac cone on the surface, Nat. Phys. **5**, 398 (2009).

[8] C. L. Kane and E. J. Mele, Z_2 Topological Order and the Quantum Spin Hall Effect, Phys. Rev. Lett. **95**, 146802 (2005).

[9] Z.-C. Gu and X.-G. Wen, Tensor-entanglement-filtering renormalization approach and symmetry protected topological order, Phys. Rev. B **80**, 155131 (2009).

[10] F. Pollmann, E. Berg, A. M. Turner, and M. Oshikawa, Symmetry protection of topological phases in one-dimensional quantum spin systems, Phys. Rev. B **85**, 075125 (2012).

[11] X. Chen, Z.-C. Gu, and X.-G. Wen, Classification of gapped symmetric phases in 1D spin systems, Phys. Rev. B **83**, 035107 (2011).

[12] A. K. Geim and K. S. Novoselov, The rise of graphene, Nat. Mater. **6**, 183 (2007).

[13] A. K. Geim, Graphene: status and prospects, Science **324**, 1530 (2009).

[14] A. H. Castro Neto, F. Guinea, N. M. R. Peres, K. S. Novoselov, and A. K. Geim, The electronic properties of graphene, Rev. Mod. Phys. **81**, 109 (2009).

[15] Y. Ando, Topological insulator materials, J. Phys. Soc. Jpn. **82**, 102001 (2013).

[16] M. Z. Hasan and C. L. Kane, Colloquium: Topological insulators, Rev. Mod. Phys. **82**, 3045 (2010).

[17] Z. K. Liu, B. Zhou, Y. Zhang, Z. J. Wang, H. M. Weng, D. Prabhakaran, S. K. Mo, Z. X. Shen, Z. Fang, X. Dai, Z. Hussain, and Y. L. Chen, Discovery of a three-dimensional topological dirac semimetal, Na_3Bi, Science **343**, 864 (2014).

[18] M. Neupane, S. Y. Xu, R. Sankar, N. Alidoust, G. Bian, C. Liu, I. Belopolski, T. R. Chang, H. T. Jeng, H. Lin, A. Bansil, F. Chou, and M. Z. Hasan, Observation of a three dimensional topological Dirac semimetal phase in high mobility Cd_3As_2, Nat. Commun. **5**, 3786 (2014).

[19] S. Y. Xu, I. Belopolski, N. Alidoust, M. Neupane, G. Bian, C. Zhang, R. Sankar, G. Chang, Z. Yuan, C. C. Lee, S. M. Huang, H. Zheng, J. Ma, D. S. Sanchez, B. Wang, A. Bansil, F. Chou, P. P. Shibayev, H. Lin, S. Jia, and M. Z. Hasan, Discovery of a Weyl fermion semimetal and topological Fermi arcs, Science **349**, 613 (2015).

[20] A. A. Soluyanov, D. Gresch, Z. Wang, Q. Wu, M. Troyer, X. Dai, and B. A. Bernevig, Type-II Weyl semimetals, Nature (London) **527**, 495 (2015).

[21] Q. Xu, Z. Song, S. Nie, H. Weng, Z. Fang, and X. Dai, Two-dimensional oxide topological insulator with iron pnictide superconductor LiFeAs structure, Phys. Rev. B **92**, 205310 (2015).

[22] G. Bian, T.-R. Chang, H. Zheng, S. Velury, S.-Y. Xu, T. Neupert, C.-K. Chiu, S. M. Huang, D. S. Sanchez, I. Belopolski, N. Alidoust, P.-J. Chen, G. Chang, A. Bansil, H. T. Jeng, H. Lin, and M. Z. Hasan, Drumhead surface states and topological nodal-line fermions in $TlTaSe_2$, Phys. Rev. B **93**, 121113(R) (2016).

[23] S.-M. Huang, S.-Y. Xu, I. Belopski, C.-C. Lee, G. Chang, T.-R. Chang, B. Wang, N. Alidoust, G. Bian, M. Neupane, D. Sanchez, H. Zheng, H.-T. Jeng, A. Bansil, T. Neupert, H. Lin, and M. Z. Hasan, New type of Weyl semimetal with quadratic double Weyl fermions, Proc. Natl. Acad. Sci. U.S.A. **113**, 1180 (2016).

[24] Y. S. Hor, A. J. Williams, J. G. Checkelsky, P. Roushan, J. Seo, Q. Xu, H. W. Zandbergen, A. Yazdani, N. P. Ong, and R. J. Cava, Superconductivity in $Cu_xBi_2Se_3$ and its Implications for Pairing in Undoped Topological Insulator, Phys. Rev. Lett. **104**, 057001 (2010).

[25] T. Asaba, B. J. Lawson, C. Tinsman, L. Chen, P. Corbae, G. Li, Y. Qiu, Y. S. Hor, L. Fu, and L. Li, Rotational Symmetry Breaking in a Trigonal Superconductor Nb-doped Bi_2Se_3, Phys. Rev. X **7**, 011009 (2017).

[26] L. Fu and E. Berg, Odd-Parity Topological Superconductors: Theory and Application to $Cu_xBi_2Se_3$, Phys. Rev. Lett. **105**, 097001 (2010).

[27] J. R. Jeffries, A. L. Lima Sharma, P. A. Sharma, C. D. Spataru, S. K. McCall, J. D. Sugar, S. T. Weir, and Y. K. Vohra, Distinct superconducting states in the pressure-induced metallic structures of the nominal semimetal Bi_4Te_3, Phys. Rev. B **84**, 092505 (2011).

[28] K. Yamana, K. Kihara, and T. Matsumoto, Bismuth tellurides: BiTe and Bi_4Te_3, Acta Cryst. Sect. B **35**, 147 (1979).

[29] Z. Ren, A. A. Taskin, S. Sasaki, K. Segawa, and Y. Ando, Large bulk resistivity and surface quantum oscillations in the topological insulator Bi_2Te_2Se, Phys. Rev. B **82**, 241306(R) (2010).

[30] K. Wang, D. Graf, and C. Petrovic, Large magnetothermopower and Fermi surface reconstruction in Sb_2Te_2Se, Phys. Rev. B **89**, 125202 (2014).

[31] J. Reimann, J. Güdde, K. Kuroda, E. V. Chulkov, and U. Hofer, Spectroscopy and dynamics of unoccupied electronic states of the topological insulators Sb_2Te_3 and Sb_2Te_2S, Phys. Rev. B **90**, 081106(R) (2014).

[32] H. Lin, T. Das, L. A. Wray, S.-Y. Xu, M. Z. Hasan, and A. Bansil, An isolated Dirac cone on the surface of ternary tetradymite-like topological insulators, New J. Phys. **13**, 095005 (2011).

[33] A. Collaudin, B. Fauqué, Y. Fuseya, W. Kang, and K. Behnia, Angle Dependence of the Orbital Magnetoresistance in Bismuth, Phys. Rev. X **5**, 021022 (2015).

[34] H. Ji, I. Pletikosic, Q. D. Gibson, G. Sahasrabudhe, T. Valla, and R. J. Cava, Strong topological metal material with multiple Dirac cones, Phys. Rev. B **93**, 045315 (2016).

[35] K. W. Chen, S. Das, D. Rhodes, S. Memaran, T. Besara, T. Siegrist, E. Manousakis, L. Balicas, and R. E. Baumbach, Uncovering the behavior of Hf_2Te_2P and the candidate Dirac metal Zr_2Te_2P, J. Phys.: Condens. Matter **28**, 14LT01 (2016).

[36] See Supplemental Material at http://link.aps.org/supplemental/10.1103/PhysRevB.97.165112 for brief description, which includes Refs. [52–62].

[37] A. Kokalj, Computer graphics and graphical user interfaces as tools in simulations of matter at the atomic scale, Comput. Mater. Sci. **28**, 155 (2003).

[38] L. Fu and C. L. Kane, Topological insulators with inversion symmetry, Phys. Rev. B **76**, 045302 (2007).

[39] M. Bianchi, D. Guan, S. Bao, J. Mi, B. B. Iversen, P. D. C. King, and P. Hofmann, Coexistence of the topological state and a two-dimensional electron gas on the surface of Bi_2Se_3, Nat. Commun. **1**, 128 (2010).

[40] E. Frantzeskakis, N. de Jong, B. Zwartsenberg, T. V. Bay, Y. K. Huang, S. V. Ramankutty, A. Tytarenko, D. Wu, Y. Pan, S. Hollanders, M. Radovic, N. C. Plumb, N. Xu, M. Shi, C. Lupulescu, T. Arion, R. Ovsyannikov, A. Varykhalov, W. Eberhardt, A. de Visser, E. van Heumen, and M. S. Golden, Dirac states with knobs on: Interplay of external parameters and the surface electronic properties of three-dimensional topological insulators, Phys. Rev. B **91**, 205134 (2015).

[41] Y. Xu, I. Miotkowski, C. Liu, J. Tian, H. Nam, N. Alidoust, J. Hu, C.-K. Shih, M. Z. Hasanand, and Y. P. Chen, Observation of topological surface state quantum Hall effect in an intrinsic three-dimensional topological insulator, Nat. Phys. **10**, 956 (2014).

[42] L. Fu and C. L. Kane, Superconducting Proximity Effect and Majorana Fermions at the Surface of a Topological Insulator, Phys. Rev. Lett. **100**, 096407 (2008).

[43] M. J. Panzer, C. R. Newman, and C. D. Frisbie, Low-voltage operation of a pentacene field-effect transistor with a polymer electrolyte gate dielectric, Appl. Phys. Lett. **86**, 103503 (2005).

[44] H. Shimotani, H. Asanuma, J. Takeya, and Y. Iwasa, Electrolyte gated charge accumulation in organic single crystals, Appl. Phys. Lett. **89**, 203501 (2006).

[45] S. Y. Guan, P. Jen Chen, M. W. Chu, R. Sankar, F. Chou, H. T. Jeng, C. S. Chang, and T. M. Chuang, Superconducting topological surface states in the noncentrosymmetric bulk superconductors PbTaSe2, Sci. Adv. **2**, e1600894 (2016).

[46] A. R. Mellnik, J. S. Lee, A. Richardella, J. L. Grab, P. J. Mintun, M. H. Fisher, A. Vaezi, A. Manchin, E. A. Kim, N. Samarth, and D. C. Ralph, Spin-transfer torque generated by a topological insulator, Nature (London) **511**, 449 (2014).

[47] Y. Baum, T. Posske, I. C. Fulga, B. Trauzettel, and A. Stern, Coexisting Edge States and Gapless Bulk in Topological States of Matter, Phys. Rev. Lett. **114**, 136801 (2015).

[48] M. Hoesch, M. Muntwiler, V. N. Petrov, M. Hengsberger, L. Patthey, M. Shi, M. Falub, T. Greber, and J. Osterwalder, Spin structure of the Shockley surface state on Au(111), Phys. Rev. B **69**, 241401(R) (2004).

[49] I. Barke and H. Hovel, Confined Shockley Surface States on the (111) Facets of Gold Clusters, Phys. Rev. Lett. **90**, 166801 (2003).

[50] E. C. H. Sykes, P. Han, S. A. Kandel, K. F. Kelly, G. S. McCarty, and P. S. Weiss, Substrate-mediated interactions and intermolecular forces between molecules adsorbed on surfaces, Acc. Chem. Res. **36**, 945 (2003).

[51] K. M. Andrews and T. P. Pearl, Modification of Ag(111) surface electronic structure via weak molecular adsorption of adenine measured with low temperature scanning tunneling microscopy and spectroscopy, J. Chem. Phys. **132**, 214701 (2010).

[52] D. Shoenberg, *Magnetic Oscillations in Metals* (Cambridge University Press, Cambridge, England, 1984).

[53] G. Kresse and J. Hafner, *Ab initio* molecular dynamics for liquid metals, Phys. Rev. B **47**, 558 (1993).

[54] G. Kresse and J. Hafner, *Ab initio* molecular-dynamics simulation of the liquid-metal-amorphous-semiconductor transition in germanium, Phys. Rev. B **49**, 14251 (1994).

[55] G. Kresse and J. Furthmüller, Efficiency of ab-initio total energy calculations for metals and semiconductors using a plane-wave basis set, Comput. Mater. Sci. **6**, 15 (1996).

[56] G. Kresse and J. Furthmüller, Efficient iterative schemes for ab initio total-energy calculations using a plane-wave basis set, Phys. Rev. B **54**, 11169 (1996).

[57] J. P. Perdew, K. Burke, and M. Ernzerhof, Generalized Gradient Approximation Made Simple, Phys. Rev. Lett. **77**, 3865 (1996).

[58] P. E. Blöchl, Projector augmented-wave method, Phys. Rev. B **50**, 17953 (1994).

[59] P. Giannozzi *et al.*, QUANTUM ESPRESSO: a modular and open-source software project for quantum simulations of materials, J. Phys.: Condens. Matter **21**, 395502 (2009).

[60] A. A. Mostofi, J. R. Yates, G. Pizzi, Y.-S. Lee, I. Souza, D. Vanderbilt, and N. Marzari, An updated version of WANNIER90: A tool for obtaining maximally-localised Wannier functions, Comput. Phys. Commun. **185**, 2309 (2014).

[61] K. Schwarz, P. Blaha, and G. Madsen, Electronic structure calculations of solids using the WIEN2K package for material sciences, Comput. Phys. Commun. **147**, 71 (2002).

[62] D. R. Hamann, Optimized norm-conserving Vanderbilt pseudopotentials, Phys. Rev. B **88**, 085117 (2013).